
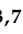



Article

Improving the CO and CH₄ Gas Sensor Response at Room Temperature of α -Fe₂O₃(0001) Epitaxial Thin Films Grown on SrTiO₃(111) Incorporating Au(111) Islands

Aída Serrano^{1,2,3,*}, Jesús López-Sánchez^{2,3,4}, Iciar Arnay^{2,3}, Rosalía Cid^{2,3,5}, María Vila^{2,3,6}, Eduardo Salas-Cólera^{2,3,7}, Germán R. Castro^{2,3} and Juan Rubio-Zuazo^{2,3}

¹ Instituto de Cerámica y Vidrio (ICV), Consejo Superior de Investigaciones Científicas (CSIC), 28049 Madrid, Spain

² Spanish CRG BM25 Beamline-SpLine at the European Synchrotron Radiation Facility (ESRF), 38000 Grenoble, France; lopezsan@esrf.fr (J.L.-S.); iciar.arnay@imdea.org (I.A.); rcid@cicenergigune.com (R.C.); maria.vila@urjc.es (M.V.); edusc22@gmail.com (E.S.-C.); german.castro@esrf.fr (G.R.C.); juan.rubio@esrf.fr (J.R.-Z.)

³ Instituto de Ciencia de Materiales de Madrid (ICMM), Consejo Superior de Investigaciones Científicas (CSIC), 28049 Madrid, Spain

⁴ Departamento de Física de Materiales, Universidad Complutense de Madrid, 28040 Madrid, Spain

⁵ Centre for Cooperative Research on Alternative Energies (CIC energiGUNE), Basque Research and Technology Alliance (BRTA), Alava Technology Park, 01510 Vitoria-Gasteiz, Spain

⁶ Escuela Técnica Superior de Ingeniería de Telecomunicación (ETSIT), Universidad Rey Juan Carlos, 28933 Madrid, Spain

⁷ Departamento de Física, Universidad Carlos III de Madrid (UC3M), Leganés, 28911 Madrid, Spain

* Correspondence: aida.serrano@csic.es

Citation: Serrano, A.; López-Sánchez, J.; Arnay, I.; Cid, R.; Vila, M.;

Salas-Cólera, E.; Castro, G.R.; Rubio-Zuazo, J. Improving the CO and CH₄ Gas Sensor Response at Room Temperature of α -Fe₂O₃(0001) Epitaxial Thin Films Grown on SrTiO₃(111) Incorporating Au(111) Islands. *Coatings* **2021**, *11*, 848. <https://doi.org/10.3390/coatings11070848>

Academic Editor: Angela De Bonis

Received: 18 June 2021

Accepted: 8 July 2021

Published: 14 July 2021

Publisher's Note: MDPI stays neutral with regard to jurisdictional claims in published maps and institutional affiliations.



Copyright: © 2021 by the authors. Licensee MDPI, Basel, Switzerland. This article is an open access article distributed under the terms and conditions of the Creative Commons Attribution (CC BY) license (<https://creativecommons.org/licenses/by/4.0/>).

Abstract: In this work, the functional character of complex α -Fe₂O₃(0001)/SrTiO₃(111) and Au(111) islands/ α -Fe₂O₃(0001)/SrTiO₃(111) heterostructures has been proven as gas sensors at room temperature. Epitaxial Au islands and α -Fe₂O₃ thin film are grown by pulsed laser deposition on SrTiO₃(111) substrates. Intrinsic parameters such as the composition, particle size and epitaxial character are investigated for their influence on the gas sensing response. Both Au and α -Fe₂O₃ layer show an island-type growth with an average particle size of 40 and 62 nm, respectively. The epitaxial and incommensurate growth is evidenced, confirming a rotation of 30° between the in-plane crystallographic axes of α -Fe₂O₃(0001) structure and those of SrTiO₃(111) substrate and between the in-plane crystallographic axes of Au(111) and those of α -Fe₂O₃(0001) structure. α -Fe₂O₃ is the only phase of iron oxide identified before and after its functionalization with Au nanoparticles. In addition, its structural characteristics are also preserved after Au deposition, with minor changes at short-range order. Conductance measurements of Au(111)/ α -Fe₂O₃(0001)/SrTiO₃(111) system show that the incorporation of epitaxial Au islands on top of the α -Fe₂O₃(0001) layer induces an enhancement of the gas-sensing activity of around 25% under CO and 35% under CH₄ gas exposure, in comparison to a bare α -Fe₂O₃(0001) layer grown on SrTiO₃(111) substrates. In addition, the response of the heterostructures to CO gas exposure is around 5–10% higher than to CH₄ gas in each case.

Keywords: Au/ α -Fe₂O₃ heterostructure; island-type growth; epitaxial growth; surface functionalization; gas sensor activity

1. Introduction

CH₄ is the main component of natural gas and is widely employed in industrial production [1]. This compound, along with CO, is usually generated through coal spontaneous combustion, and both represent a real danger for human life and climate change [1,2]. Hence, the development of gas sensors capable of monitoring CH₄ and CO leakage is essential in the current society to ensure a safer and healthier environment. In this line, metal oxide semiconductors are the most attractive materials for gas sensors since they are

chemically stable and can change their resistance when a specific gas interacts with their surface [3,4]. These properties render the metal oxide semiconductor-based gas sensors as very viable alternatives compared to the conventional analytical techniques in order to achieve high sensing performance [2]. However, the exploitation of these gas sensors is limited to factors such as the high costs of certain semiconductors and the high temperatures for a good operation [3].

Specifically, α -Fe₂O₃ (hematite) has been used as gas sensor in many applications due to its interesting properties such as its low toxicity, stability under ambient conditions and low costs [5–7]. α -Fe₂O₃ is one of the most abundant minerals and probably one of the most used iron oxides. Its morphological forms can be assorted controlling the physical properties, which allows employing this iron oxide polymorph in different fields as magnetic data storage technologies, biomedicine, catalysis or gas sensors [5,8–12], demonstrating its high-potential. For example, for water splitting applications, α -Fe₂O₃ has been considered as an active oxide for CO oxidation at low temperature [13,14]. In addition, a larger photochemical reactivity has been identified in α -Fe₂O₃ surfaces grown on SrTiO₃(111) substrates [15]. As a gas sensor, α -Fe₂O₃ has been also continuously investigated for monitoring combustible or toxic gases. Mesoporous nanoparticles, nanoporous nanoparticles, hollow balls, thin films and single-crystalline oblique nanoparallelepipeds, among others, are some of the configurations employed with reported gas sensing properties [4,16–21].

The incorporation of certain nanoparticles on active surfaces allows enhancing their physical properties for a wide range of attractive applications. In this respect, the functionalization of α -Fe₂O₃ surfaces with noble metallic nanoparticles has been proven to improve, for example, the catalytic activities [3,4,22–24]. However, the transfer of this type of nanoparticles, without modifying their characteristics and properties, is not an easy way and considerable efforts have been expended on it. A common and interesting approach that allows covering large surfaces with functional nanoparticles is the solid state dewetting [25–28]. Based on this processing method, a one-step strategy has been reported in which noble metal nanostructures are prepared on an oxide support by the deposition of metallic material with the substrate at a specific temperature [29–31]. This approach avoids a subsequent annealing process after the deposition of a metallic film [25–27,32] and, to the best of our knowledge, it has been used to obtain Au and Pt nanoparticles on iron oxide surfaces [29,31] and Al nanostructures on Si and glass substrates [30]. Using this methodology, we have recently investigated the effect of the substrate temperature and the type of the substrate in the preparation of Au nanostructures on α -Fe₂O₃ surfaces, reporting a precise control of the morphological characteristics of the noble metal nanostructures tuning accurately the growth parameters [31].

In this work, considering these premises, we have studied the incorporation of Au nanoparticles on α -Fe₂O₃ thin films grown on SrTiO₃(111) substrates and the gas sensing properties of the complex systems for CO and CH₄ gases. Several morphological and structural parameters of nanomaterials, such as the composition, particle size, area exposed or the epitaxial character, among others, influence the gas sensor response. Therefore, an exhaustive morphological, structural and compositional characterization of α -Fe₂O₃/SrTiO₃(111) and Au/ α -Fe₂O₃/SrTiO₃(111) heterostructures has been carried out, examining specifically the α -Fe₂O₃ features before and after its surface functionalization with Au islands. In addition, conductance experiments are presented, showing the gas sensing performance of complex systems under CO and CH₄ atmospheres and the enhancement of response on the functionalized epitaxial α -Fe₂O₃ layers when epitaxial Au nanostructures are incorporated on top.

2. Materials and Methods

α -Fe₂O₃ thin films and Au nanoparticles/ α -Fe₂O₃ heterostructures were grown on SrTiO₃ (STO)(111) substrates by pulsed laser deposition according to a previous work [31]. The growth was performed by using an ultraviolet pulsed laser source (355 nm) of high power (1 W) to obtain the plasma, with a base pressure of 10^{−9} mbar. α -Fe₂O₃ thin films

were deposited on the substrates at 400 °C using an α -Fe₂O₃ target under an O₂ atmosphere (oxygen pressure, P_{O₂}, of 10⁻⁴ mbar), while Au nanoparticles were grown from a Au target on α -Fe₂O₃ films keeping the P_{O₂} about 10⁻⁴ mbar, in order to prevent the reduction to Fe₃O₄, and with the sample kept at 250 °C.

During the deposition process, the crystalline character of both layers was analyzed by in situ reflection high-energy electron diffraction (RHEED) using a primary electron beam of 29 keV. Morphology of the samples was studied by scanning electron microscopy (SEM) with an S-4700 Hitachi instrument (Hitachi, Marunouchi, Chiyoda-ku, Tokyo, Japan) at 20 kV and morphological features were examined by using the software ImageJ (Version 1.51).

Grazing incidence X-ray diffraction (GIXRD), X-ray reflectivity (XRR) and X-ray absorption spectroscopy (XAS) experiments were carried out at the Spanish CRG synchrotron beamline BM25-SpLine at the European Synchrotron Radiation Facility (ESRF), in Grenoble (France). GIXRD and XRR measurements were carried out in a high precision six-circle diffractometer (HUBER Diffraktionstechnik GmbH & Co. KG, Rimsting, Germany) in vertical geometry [33] at room temperature using a photon wavelength of 0.826 Å (hν = 15 keV) to ensure the access to a wide reciprocal space region. XAS experiments were performed at the Fe K-edge (7112 eV) at room temperature in fluorescence mode using a 13-elements Si(Li) detector from e2V Scientific Instruments (Sirius House, Watery Lane, Wooburn Green, High Wycombe, Buckinghamshire, UK) located 90° with respect to the incoming X-ray beam. Spectra of reference standards (Fe foil, FeO, Fe₃O₄ and α -Fe₂O₃) were measured for comparison in transmission mode with two ionization chambers as detectors. XAS data were analyzed using Demeter package (Version 0.9.26) [34,35].

X-ray photoelectron spectroscopy (XPS) measurements were carried out on the Fe 2p and Au 4f core levels using a standard monochromatic X-ray tube with a Mg K α radiation anode (hν = 1253.6 eV). The binding energy of XPS spectra was calibrated considering the C 1s binding energy of a small residual amount at 284.8 eV.

The gas sensing characteristics of the samples were measured in a home-made chamber for CO and CH₄ gas at room temperature in a continuous gas flux mode. Gases were injected into the chamber separately through a precision leak valve and the gas concentration was regulated by mass flux controllers adjusting the flow rates of gases. The flow inside the chamber was set to 1 bar with a gas flux of 50 mL/min and a gas concentration of 3000 mg/m³. During the experiments, gas sensor tests were performed at a relative humidity (RH) of 40(10)%. Sensor conductance measurements were normalized by the response recorded without gas under a base pressure around 10⁻² mbar into the chamber. A multimeter from Keithley instruments (Model 6514, Cleveland, OH, USA) was employed to collect the resistance measurement applying a bias voltage of 10 V. A scheme representing the experimental setup used for gas sensor measurements in real time is shown in Figure 1.

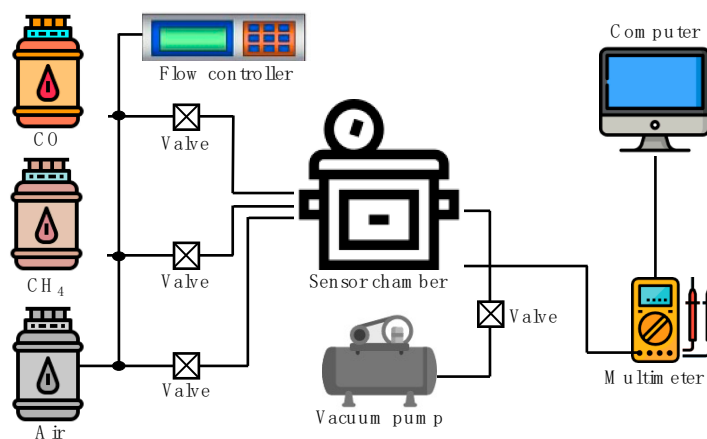


Figure 1. Experimental setup used to carry out gas sensor experiments in real time.

3. Results

3.1. Morphological and Structural Characterization

During the growth process of both α -Fe₂O₃ and Au layers by pulsed laser deposition, in situ RHEED technique was employed to monitor their crystalline character. From the initial stages of deposition, intense patterns were observed. Figure 2 shows representative RHEED patterns of the clean STO(111) substrate and those of α -Fe₂O₃ thin film grown on STO(111) and Au islands grown on α -Fe₂O₃/STO(111) system at the final growth stages. In both Au and α -Fe₂O₃ layers, the RHEED patterns show smooth diffraction stripes, related to the growth of homogeneous and crystalline films.

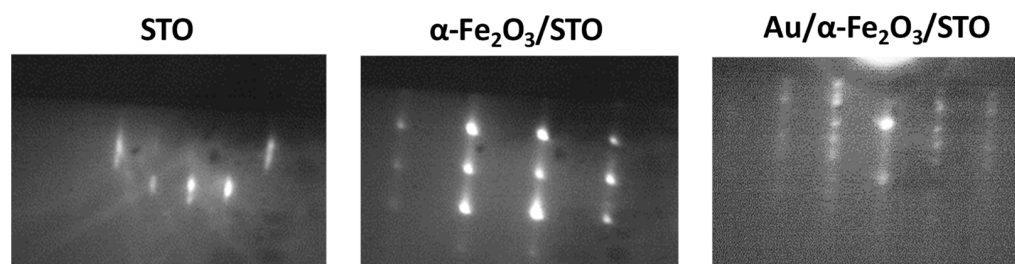


Figure 2. Representative RHEED patterns of the clean STO(111) substrate, α -Fe₂O₃ thin films grown on STO(111) substrate and Au islands grown on α -Fe₂O₃/STO(111) system. During the deposition process of both α -Fe₂O₃ and Au layers, intense patterns with smooth diffraction stripes are identified.

Figure 3 shows the SEM images and the distribution analysis of particle size for α -Fe₂O₃ thin film and Au/ α -Fe₂O₃ bilayer prepared on oxide STO(111) substrate. α -Fe₂O₃ thin film grown on STO(111) (Figure 3a) shows a homogeneous coverage of particles with an average size about 62(2) nm (Figure 3c), identifying an island-type growth. The greater interaction of α -Fe₂O₃ atoms with those of the STO substrate generates the formation of a α -Fe₂O₃ layer with a nanoparticulate character in order to minimize the system free energy. For the case of the Au/ α -Fe₂O₃ bilayer, a nanostructured top layer related to the formation of Au islands is obtained on α -Fe₂O₃/STO(111) system. Au islands also show a homogeneous coverage on α -Fe₂O₃ surface, with an average particle size of 40(2) nm (see Figure 3b,d). This type of growth is induced during the Au growth when the sample substrate is kept at a temperature of 250 °C, as was identified previously in [31], inducing an island-type growth of Au promoted by the surface diffusion. The phenomenon is attributed to a dewetting process by a one-step procedure, instead of the usual methodology based on the post-annealing of the metallic film [25–28,32,36]. Specifically here, the α -Fe₂O₃ surface presents a particulate character with a discontinuous profile, which generates a more heterogeneous stress distribution than in a flat surface. These features of the bottom layer favor the nucleation of Au holes and the formation of larger and more separated Au islands in order to minimize the interface energy of the system [37], with qualitative similar final results. The average height for both α -Fe₂O₃ and Au layers was also determined on equivalent samples in our previous works to be 2.3(4) nm and 6(1) nm, respectively, by atomic force microscopy (AFM) and GIXRD [31,38].

To analyze the in-plane and out-plane crystalline growth of the Au and α -Fe₂O₃ layer, high resolution GIXRD, XRR, and reciprocal space map (RSM) measurements were performed. From low angle XRR measurements of the α -Fe₂O₃ layer and Au/ α -Fe₂O₃ bilayer deposited on oxide STO(111), shown in Figure 4a, the thicknesses of the layers were estimated using the period of the oscillations. A thickness of 28(2) nm for the α -Fe₂O₃ layers and 6(1) nm for the Au layer was obtained. Representative high angle XRR measurements for the α -Fe₂O₃ layer and Au/ α -Fe₂O₃ bilayer grown on STO(111) substrates are shown in Figure 4b. In the α -Fe₂O₃/STO(111) system, in addition to the diffraction peak corresponding to the STO(111) substrate, the presence of α -Fe₂O₃ with (0001) orientation as a single phase is identified, which is not clearly recognized in the diffraction pattern of the Au/ α -Fe₂O₃ bilayer. In the case of the Au/ α -Fe₂O₃ bilayer,

the Au nanostructured layer on top of the α -Fe₂O₃ layer is recognized as a wide peak at lower 2θ values than the diffraction peak related to the α -Fe₂O₃ layer, which corresponds to epitaxial Au with a (111) orientation and is responsible for masking the diffraction peak signal related to the epitaxial α -Fe₂O₃ layer. It should be pointed out that some Kiessig fringes around the layer Bragg peaks can be noted, indicating the occurrence of high quality and smooth surfaces with abrupt α -Fe₂O₃/STO substrate and Au/ α -Fe₂O₃ interfaces. These results are in agreement with results reported in [31].

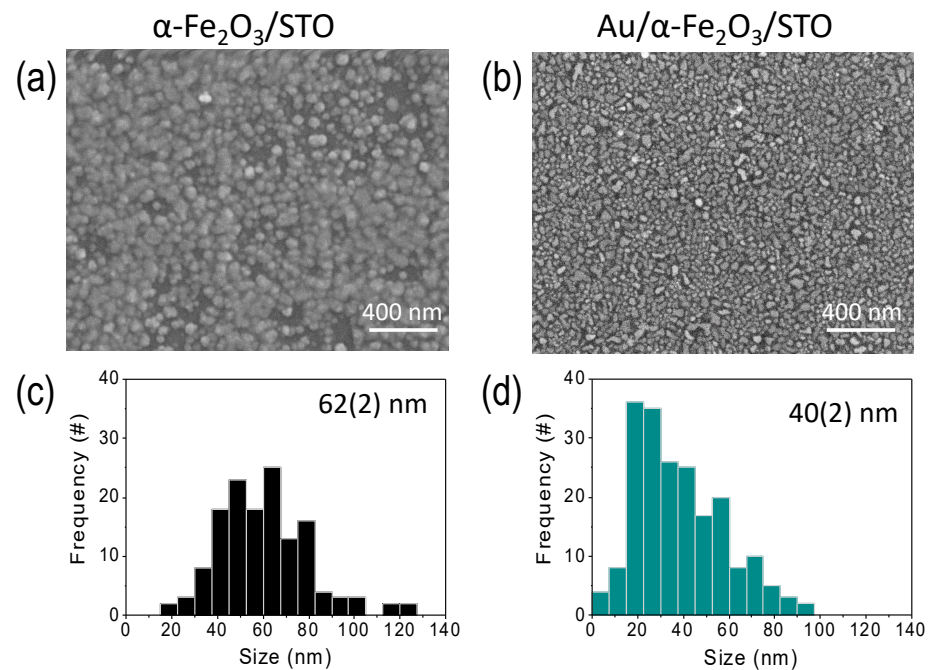


Figure 3. (a,b) SEM images and (c,d) particle size distribution analysis of α -Fe₂O₃ layer and Au/ α -Fe₂O₃ bilayer grown on STO(111) substrates. An island-type growth for α -Fe₂O₃ and Au layers is recognized with a homogeneous coverage of particles.

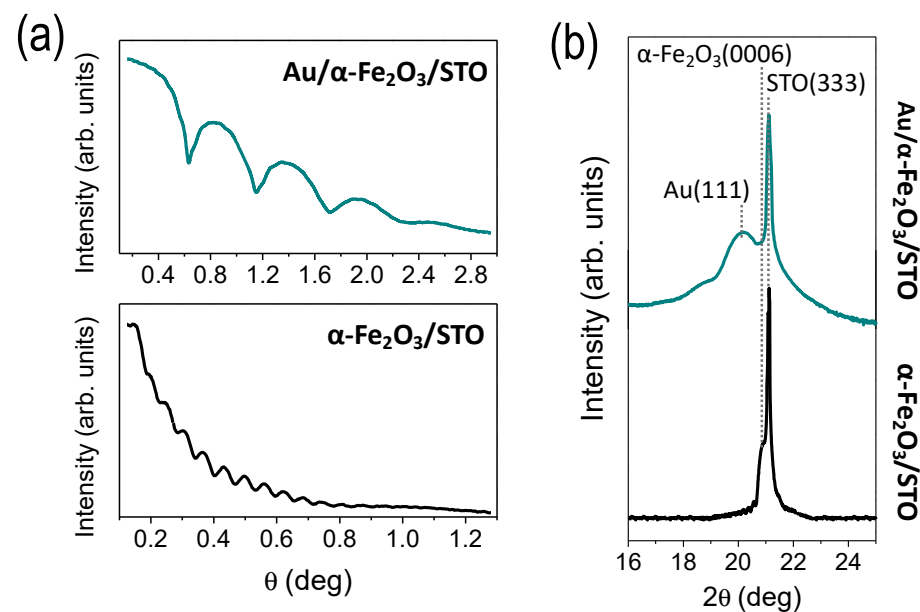


Figure 4. (a) Low angle XRR and (b) high-angle θ - 2θ scans of epitaxial α -Fe₂O₃ layer and Au/ α -Fe₂O₃ system grown on STO(111) substrates. Thicknesses were calculated to be 28(2) nm for the α -Fe₂O₃ layer and 6(1) nm for the Au layer. Bragg peaks related to STO(111) substrate, Au(111) and α -Fe₂O₃(0001) are identified.

Representative RSM measurements for the single $\alpha\text{-Fe}_2\text{O}_3$ layer and Au/ $\alpha\text{-Fe}_2\text{O}_3$ bilayer grown on STO(111) substrates are displayed in Figure 5. Taking into account the analysis of RSM measurements, an incommensurate growth based on the non-coincidence of the in-plane diffraction peak maxima from both Au and $\alpha\text{-Fe}_2\text{O}_3$ layers and the STO substrate is recognized. Besides, the crystallographic coupling between the layers and the substrate is analyzed. A rotation of 30° is shown between the in-plane crystallographic axes of the $\alpha\text{-Fe}_2\text{O}_3$ layer and the STO(111) substrate and the Au layer and the $\alpha\text{-Fe}_2\text{O}_3$ layer, with the crystallographic axes between Au and STO substrate parallel. Thus, the orientation relationships between the lattices of Au and $\alpha\text{-Fe}_2\text{O}_3$ layers and the STO substrate is: $(0001)[100]_{\alpha\text{-Fe}_2\text{O}_3} \parallel (111)[110]_{\text{STO}}$ for $\alpha\text{-Fe}_2\text{O}_3/\text{STO}(111)$ and $(111)[110]_{\text{Au}} \parallel (0001)[100]_{\alpha\text{-Fe}_2\text{O}_3} \parallel (111)[110]_{\text{STO}}$ for Au/ $\alpha\text{-Fe}_2\text{O}_3/\text{STO}(111)$ system, as previously reported [31,38].

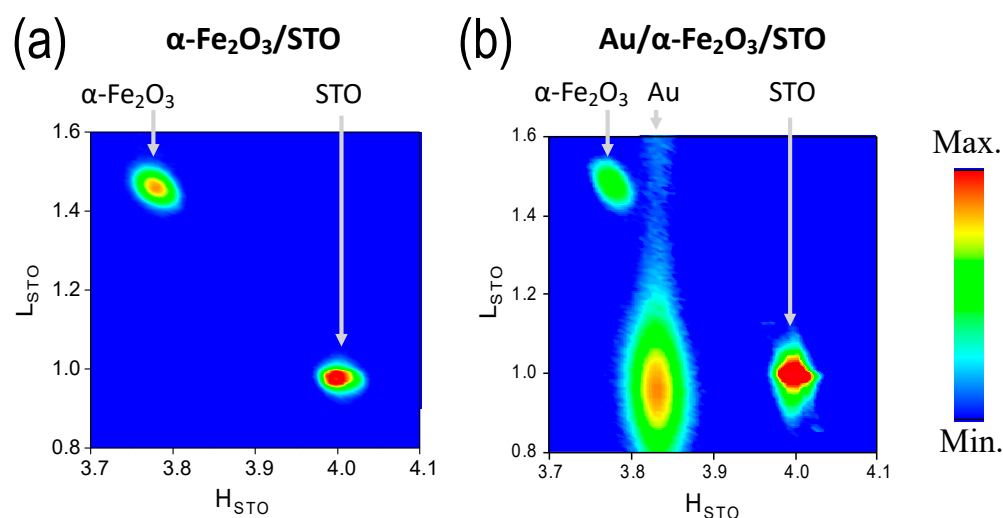


Figure 5. LH reciprocal space maps (RSM) for (a) $\alpha\text{-Fe}_2\text{O}_3$ layer grown on STO(111) substrate and (b) Au/ $\alpha\text{-Fe}_2\text{O}_3$ bilayer prepared on STO(111) substrates. An incommensurate epitaxial growth is identified from a non-coincidence of Au(111), $\alpha\text{-Fe}_2\text{O}_3$ (0001), and STO(111) substrate in-plane peaks (marked in each figure). The color scale corresponds to the signal intensity.

Out-of-plane and in-plane lattice parameters were calculated from the positions at several diffraction peaks in reciprocal space respect to the STO(111) substrate obtaining for $\alpha\text{-Fe}_2\text{O}_3$ layers: $c_{\alpha\text{-Fe}_2\text{O}_3/\text{STO}} = 13.72(6)$ Å, $c_{\text{Au}/\alpha\text{-Fe}_2\text{O}_3/\text{STO}} = 13.72(3)$ Å, $a_{\alpha\text{-Fe}_2\text{O}_3} = b_{\alpha\text{-Fe}_2\text{O}_3} = 5.08(4)$ Å and $a_{\text{Au}/\alpha\text{-Fe}_2\text{O}_3/\text{STO}} = b_{\text{Au}/\alpha\text{-Fe}_2\text{O}_3/\text{STO}} = 5.07(1)$ Å and for Au layer: $c_{\text{Au}/\alpha\text{-Fe}_2\text{O}_3/\text{STO}} = 7.04(2)$ Å and $a_{\text{Au}/\alpha\text{-Fe}_2\text{O}_3/\text{STO}} = b_{\text{Au}/\alpha\text{-Fe}_2\text{O}_3/\text{STO}} = 2.89(2)$ Å. Additionally, the in-plane domain sizes were calculated to be 25(1) nm for the epitaxial $\alpha\text{-Fe}_2\text{O}_3$ layer and Au/ $\alpha\text{-Fe}_2\text{O}_3$ system and 17(1) nm for the epitaxial Au, in agreement with previous work [31]. Similar values of both the lattice crystallographic parameters and in-plane domain size are obtained in the $\alpha\text{-Fe}_2\text{O}_3$ layer before and after the deposition of Au islands, indicating no crystallographic alterations of the iron oxide structure and its thermodynamic stability during the Au growth at 250 °C. Besides, the lattice parameters match those of the bulk $\alpha\text{-Fe}_2\text{O}_3$ structure disclosing a stress-free growth of layers.

Possible $\alpha\text{-Fe}_2\text{O}_3$ modifications at short-range order during the growth of Au nanoparticles or amorphous minority phases non identified by GIXRD are analyzed by XAS experiments, as Figure 6 shows. Both X-ray absorption near-edge structure (XANES) and extended X-ray absorption fine structure (EXAFS) measurements were performed. Absorption profiles obtained by XANES measurements at the Fe K-edge of heterostructures follow the absorption features of powder $\alpha\text{-Fe}_2\text{O}_3$ reference (see Figure 6a). Fitting the XANES spectra by a linear combination of different iron oxide reference compounds (Fe, FeO, Fe_3O_4 and $\alpha\text{-Fe}_2\text{O}_3$ references) [39,40] (not shown here) confirms an oxidation state of Fe^{3+} and a 100% of $\alpha\text{-Fe}_2\text{O}_3$ phase in both $\alpha\text{-Fe}_2\text{O}_3$ layer and Au/ $\alpha\text{-Fe}_2\text{O}_3$ bilayer grown on

STO(111) substrates, corroborating the α -Fe₂O₃ phase as a single iron oxide phase before and after the epitaxial deposition of Au islands.

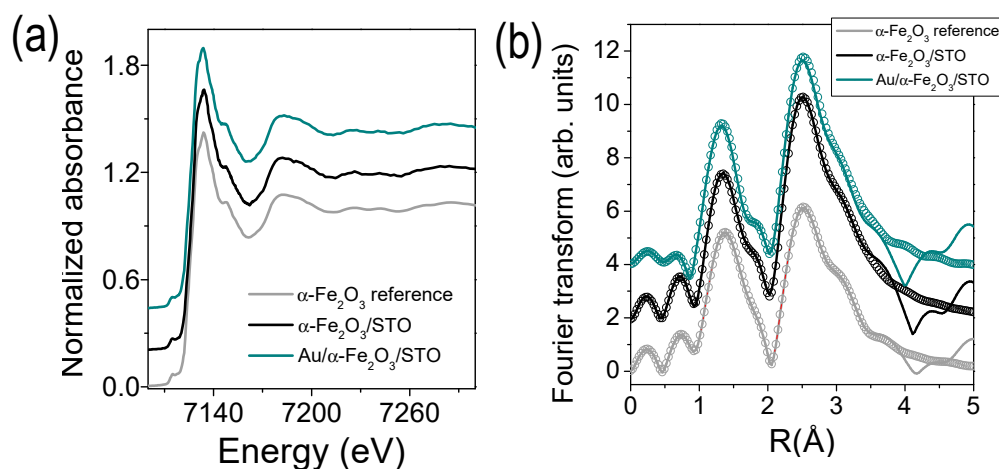


Figure 6. (a) XANES spectra and (b) FT modulus of the EXAFS signal (lines with symbols) and best-fitting simulations (continuous lines) at the Fe K-absorption edge of α -Fe₂O₃ layer and Au/ α -Fe₂O₃ bilayer grown on STO(111) substrates. XANES spectrum and FT of the EXAFS signal of α -Fe₂O₃ powder reference are presented for comparison.

The short-range ordering of cations around the Fe is studied in both α -Fe₂O₃ layer and Au/ α -Fe₂O₃ bilayer by EXAFS spectroscopy. Figure 6b shows the modulus of the Fourier transform (FT) of the EXAFS signal at the Fe K-edge. The FT is performed in the $k^2\chi(k)$ weighted EXAFS signal between 2.5 and 10.5 \AA^{-1} . Experimental EXAFS results were fitted in R-space in the range 1.0–3.6 \AA using the FEFFIT code [34]. The first intense peak involves two subshells that corresponds to a first neighbor shell with three short plus three long O neighbors around the Fe. The second peak is related to single and multiple scatterings from the nearest Fe–Fe neighbors [41]. The fitting was performed fixing the shift at the edge energy E_0 , which was previously calculated from α -Fe₂O₃ powder reference. The coordination number N , the interatomic distance R and the Debye-Waller (DW) factors σ^2 were used as free parameters for the fitting. Table 1 shows the parameters obtained from the EXAFS fittings.

In both α -Fe₂O₃/STO(111) and Au/ α -Fe₂O₃/STO(111) systems, α -Fe₂O₃ layer presents an increase of the coordination number at the five coordination shells with respect to the α -Fe₂O₃ reference (see Table 1) that may be related to the greatest local order in the epitaxial thin films. With respect to the neighbor bondlengths, both α -Fe₂O₃ layers (single and with Au islands) present an Fe–O elongation and Fe–Fe contraction, indicating a local distortion at short-range order of epitaxial α -Fe₂O₃ structure grown on the STO(111) substrate in comparison with the α -Fe₂O₃ reference. Specifically for Au/ α -Fe₂O₃/STO(111) system, most of the first neighbors present slightly larger bondlength distances than for α -Fe₂O₃/STO(111) system, which supposes a short-range order expansion that could be related to a relaxation of the α -Fe₂O₃ structure promoted by the deposition of the Au islands on the α -Fe₂O₃(0001)/STO(111) system with the substrate at 250 °C. Finally, the obtained DW factors are of similar order for both α -Fe₂O₃(0001) layers and we do not observe a structural disorder related to the growth of Au island adlayer.

The incorporation of Au islands on the α -Fe₂O₃/STO(111) system was also investigated by XPS measurements on the Fe 2p and Au 4f core level, as Figure 7 shows. The binding energy values of the Fe 2p_{3/2} peak (~710 eV) and the Fe 2p_{1/2} peak (~723.6 eV), with a distance among both of around 13.6 eV, were determined to be similar in both α -Fe₂O₃ layer and Au/ α -Fe₂O₃ bilayer and comparable to typical values reported for the Fe 2p core level [42–44]. In addition, the satellite peak of Fe 2p_{3/2} is distinguished, more clearly in the α -Fe₂O₃/STO(111) sample, and located around 8 eV higher than the main Fe

$2p_{3/2}$ peak [42–44]. These results confirm the oxidation state of the Fe cations to be Fe^{3+} and the nature of the iron oxide layer as $\alpha-Fe_2O_3$, in agreement to GIXRD and XAS results. During the XPS measurements, a lower signal is collected on the Fe 2p core level for the Au/ $\alpha-Fe_2O_3$ bilayer than that acquired from the $\alpha-Fe_2O_3$ layer due to the presence of Au islands. The Fe 2p signal is very low since the $\alpha-Fe_2O_3$ is buried 6 nm down (Au layer thickness), which is approximately the depth limit of conventional XPS equipment (see Figure 4). On the Au 4f core level, the photoemission signal related to the Au/ $\alpha-Fe_2O_3$ bilayer grown on the STO(111) substrate shows a spin–orbit splitting of 3.7 eV between Au $4f_{5/2}$ and Au $4f_{7/2}$ peaks, with $4f_{7/2}$ at 84.0 eV corresponding to that of pure Au [45,46]. Moreover, the Fe 3s signal is imperceptible with respect to that of Au 4f, which means that the nanostructured-Au layer is homogeneous and there is no segregation of Fe through the Au layer. The combination of XPS and XANES techniques demonstrates the absence of mixed Fe-Au phases present on the surface and buried interfaces.

Table 1. Results of the EXAFS fittings by a five-shell model at the Fe K-edge of $\alpha-Fe_2O_3$ layer and Au/ $\alpha-Fe_2O_3$ bilayer grown on STO(111) substrates. EXAFS parameters are compared with results obtained from powder $\alpha-Fe_2O_3$ reference.

Sample	Shell	N	R (Å)	DW(Å ²)
$\alpha-Fe_2O_3$ reference	Fe–O1	3	1.967(4)	0.006(1)
	Fe–O2	3	2.13(1)	0.017(2)
	Fe–Fe1	1	2.977(1)	0.006(1)
	Fe–Fe2	3	3.06(1)	0.007(1)
	Fe–Fe3	3	3.454(1)	0.017(1)
$\alpha-Fe_2O_3$ /STO	Fe–O1	3.4(2)	1.981(8)	0.003(1)
	Fe–O2	3.4(2)	2.188(3)	0.014(1)
	Fe–Fe1	1.2(1)	2.90(4)	0.032(9)
	Fe–Fe2	3.6(3)	2.983(2)	0.003(1)
	Fe–Fe3	3.6(3)	3.380(2)	0.005(1)
Au/ $\alpha-Fe_2O_3$ /STO	Fe–O1	3.7(2)	1.993(6)	0.003(1)
	Fe–O2	3.7(2)	2.230(5)	0.013(2)
	Fe–Fe1	1.2(1)	2.82(6)	0.032(9)
	Fe–Fe2	3.6(3)	3.001(3)	0.004(2)
	Fe–Fe3	3.6(3)	3.394(4)	0.005(1)

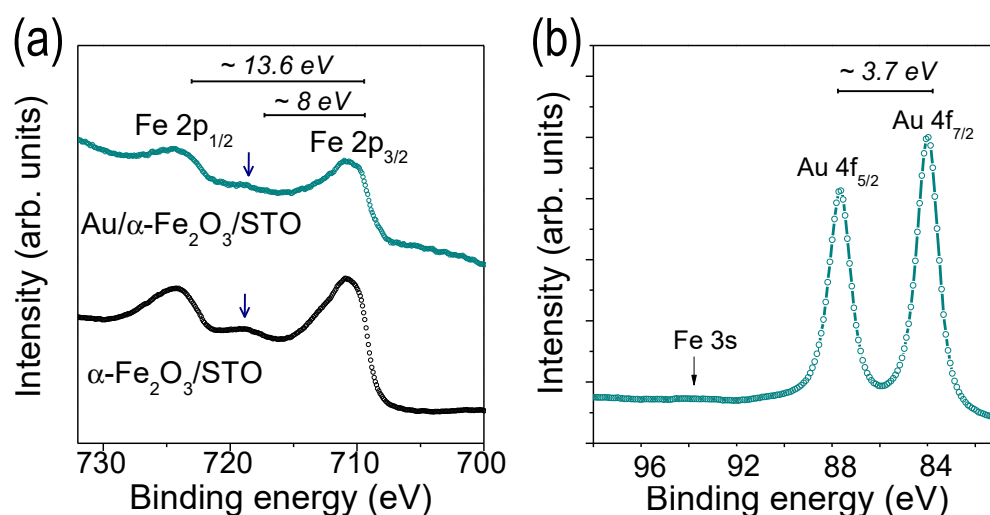


Figure 7. XPS measurements performed on the (a) Fe 2p core level of the $\alpha-Fe_2O_3$ layer and the Au/ $\alpha-Fe_2O_3$ bilayer grown on STO(111) substrates and (b) Au 4f core level of the Au/ $\alpha-Fe_2O_3$ bilayer grown on STO(111) substrate. Lower signal is collected on the Fe 2p core level for the Au/ $\alpha-Fe_2O_3$ bilayer than for the $\alpha-Fe_2O_3$ layer.

3.2. Conductance Response

The sensibility of the α -Fe₂O₃ layer and complex Au/ α -Fe₂O₃ bilayer as gas sensing materials under CO and CH₄ gas atmospheres at room temperature is shown in Figure 8. For that, the relative conductance response ($\Delta G/G_0$) of the complex Au/ α -Fe₂O₃ system is compared in each case with the results obtained for the single α -Fe₂O₃ layer deposited on the STO(111) substrate under the same conditions. In each case, the gas sensor sensibility is determined by the gas in–gas out difference from the $\Delta G/G_0$ curves. α -Fe₂O₃ is a n-type semiconductor and its gas response involves the formation of an electron depletion layer at the surface and the return of these electrons to the conduction band, increasing the conductance signal after exposure to reducing gases [18,21,47].

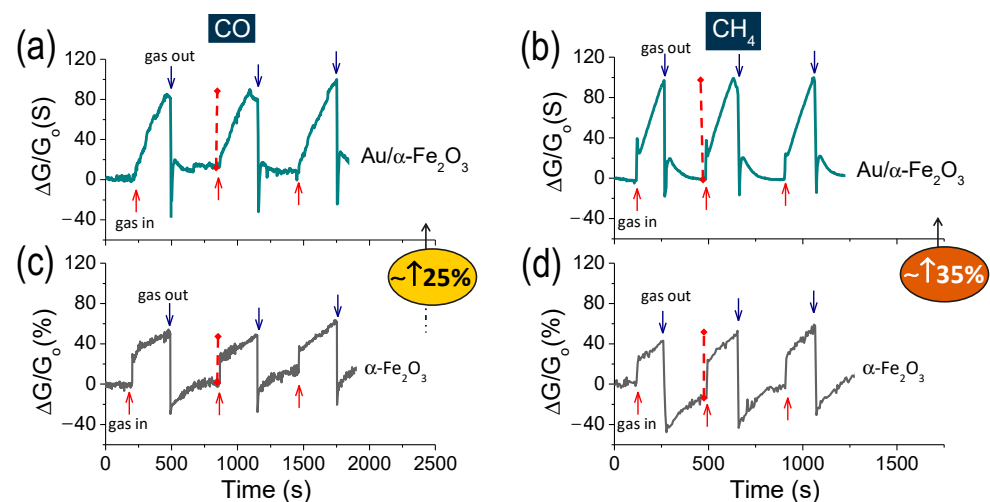


Figure 8. Gas sensor response curves for (a,b) Au/ α -Fe₂O₃ bilayers deposited on STO(111) substrate at a substrate temperature for the Au growth of 250 °C and (c,d) bare α -Fe₂O₃ thin film under (a,c) CO and (b,d) CH₄ atmosphere at room temperature. G_0 and G values correspond to the sensor conductance in air and specific gas atmosphere. The gas in to gas out difference in the $\Delta G/G_0$ curves is used to determine the gas sensor sensibility. A red bar is represented as an example in each case.

On α -Fe₂O₃/STO(111) system in contact with air, oxygen molecules are adsorbed at the α -Fe₂O₃ surface. When the gas passes through the α -Fe₂O₃ surface, it is chemisorbed at the surface with previously adsorbed oxygen and an oxidation reaction occurs. Therefore, the trapped electrons on the surface are released back to the conduction band producing an increase of the electrical conductance of α -Fe₂O₃, as shown in Figure 8 for the measurements performed at room temperature. Prior to the experiments, the linear behavior of the resistance signal was checked in each sample.

As the α -Fe₂O₃ is functionalized on top with epitaxial Au(111) islands, forming a complex Au/ α -Fe₂O₃ bilayer, the gas sensor sensibility increases around 25% under CO gas and around 35% under CH₄ (see Figure 8), which should be ascribed to the active Au islands that play an important role in catalyzing the surface sensing reactions [4,24]. It should be noted that in both complex Au/ α -Fe₂O₃ bilayer and single α -Fe₂O₃ layer, the sensor response for the CH₄ is higher than for the CO gas (~5–10%). In addition, variations in the curve shape of the gas sensor response and recovery are noted. These changes are related to the adsorption and desorption reaction kinetics of the process on the sensor surface (in both systems) and can explain by different parameters of the reactions, the operating temperature and the gas nature, among other factors [48,49].

Major limitations to increase the technology progress and competitiveness of gas sensors are the high cost of certain semiconductor materials and the usual high temperatures required for their operation. Here, α -Fe₂O₃ is used, which is one of the most abundant semiconductors with a low cost and its sensor response under CO and CH₄ atmospheres is stated at a very low temperature, i.e., at room temperature. In addition, the processing

method to prepare the Au(111)/Fe₂O₃(0001)/SrTiO₃(111) heterostructure is an easy way by a one-step method without post-processes and without modifying the structure and composition of the α -Fe₂O₃ semiconductor sensor. This methodology can be scaled up industrially and extrapolated to other catalytic systems or gas sensor systems with complementary properties. Therefore, these results are very promising for gas sensor applications at room temperature where the incorporation of epitaxial Au(111) islands on epitaxial α -Fe₂O₃(0001) layers grown on STO(111) substrates improves the gas sensor response for the detection of CO and CH₄ gas at room temperature. In addition, the complex system exhibits plasmonic activity as previously reported [31], demonstrating the multifunctional character of these hybrid Au/ α -Fe₂O₃ heterostructures.

4. Conclusions

We have grown epitaxial incommensurate α -Fe₂O₃(0001) layers and Au(111)/ α -Fe₂O₃(0001) bilayers on STO(111) substrates by pulsed layer deposition with CO and CH₄ gas sensor response at room temperature, identifying the influence of the incorporation of epitaxial Au nanostructures on the physical properties of α -Fe₂O₃ structure. An island-type growth is recognized in both Au and α -Fe₂O₃. Structurally, both before and after the Au deposition, α -Fe₂O₃ is the single iron oxide phase identified with a slight variation in the neighbor bondlengths at short-range order. The epitaxial growth is confirmed, with the in-plane crystallographic axes between Au and α -Fe₂O₃ and those between α -Fe₂O₃ and STO(111) rotated 30°. Gas sensor response under CO and CH₄ atmospheres is measured at room temperature in both α -Fe₂O₃/STO(111) and Au(111)/ α -Fe₂O₃(0001)/STO(111) systems, detecting an increase of the gas-sensing activity as the α -Fe₂O₃(0001) surface is functionalized with epitaxial Au nanostructures. The gas sensor sensibility increases around 35% under CH₄ and 25% under CO gas atmosphere, being higher for the CH₄ gas than for the CO gas (~5–10%).

Author Contributions: Conceptualization, methodology, investigation, formal analysis, data curation, writing—original draft and funding acquisition, A.S.; investigation, formal analysis and review—editing, J.L.-S., I.A., R.C., M.V. and E.S.-C.; methodology, investigation, supervision, review—editing and funding acquisition, G.R.C. and J.R.-Z. All authors have read and agreed to the published version of the manuscript.

Funding: This work has been supported by the Ministerio Español de Ciencia e Innovación (MICINN) and the Consejo Superior de Investigaciones Científicas (CSIC) through the projects PIE-2010-OE-013-200014, PIE 2021-60-E-030 and RTI2018-095303-A-C52. The ESRF, MICINN and CSIC are acknowledged for the provision of synchrotron radiation facilities. A.S. acknowledges financial support from Comunidad de Madrid for an “Atracción de Talento Investigador” Contract (2017-t2/IND5395).

Institutional Review Board Statement: Not applicable.

Informed Consent Statement: Not applicable.

Data Availability Statement: The data presented in this study are openly available at [10.20944/preprints202106.0539.v1](https://doi.org/10.20944/preprints202106.0539.v1).

Acknowledgments: We especially thank Carlos Beltrán for his technical support during the experiments at the BM25 beamline at The ESRF.

Conflicts of Interest: The authors declare no conflict of interest.

References

1. Zhang, S.; Li, H.; Zhang, N.; Zhao, X.; Zhang, Z.; Wang, Y. Self-sacrificial templated formation of ZnO with decoration of catalysts for regulating CO and CH₄ sensitive detection. *Sens. Actuators B Chem.* **2021**, *330*, 129286. [[CrossRef](#)]
2. Qiu, X.; Wei, Y.; Li, J.; Zhang, E.; Li, N.; Li, C.; Wei, J. Early detection system for coal spontaneous combustion by laser dual-species sensor of CO and CH₄. *Opt. Laser Technol.* **2020**, *121*, 105832. [[CrossRef](#)]
3. Garcia-Osorio, D.; Hidalgo-Falla, P.; Peres, H.E.M.; Gonçalves, J.M.; Araki, K.; Garcia-Segura, S.; Picasso, G. Silver enhances hematite nanoparticles based ethanol sensor response and selectivity at room temperature. *Sensors* **2021**, *21*, 440. [[CrossRef](#)] [[PubMed](#)]

4. Garcia, D.; Picasso, G.; Hidalgo, P.; Peres, H.E.M.; Sun Kou, R.; Gonçalves, J.M. Sensors based on Ag-loaded hematite (α -Fe₂O₃) nanoparticles for methyl mercaptan detection at room temperature. *Anal. Chem. Res.* **2017**, *12*, 74–81. [[CrossRef](#)]
5. Mishra, M.; Chun, D.M. α -Fe₂O₃ as a photocatalytic material: A review. *Appl. Catal. A Gen.* **2015**, *498*, 126–141. [[CrossRef](#)]
6. Mirzaei, A.; Hashemi, B.; Janghorban, K. α -Fe₂O₃ based nanomaterials as gas sensors. *J. Mater. Sci. Mater. Electron.* **2016**, *27*, 3109–3144. [[CrossRef](#)]
7. Ali, A.; Zafar, H.; Zia, M.; ul Haq, I.; Phull, A.R.; Ali, J.S.; Hussain, A. Synthesis, characterization, applications, and challenges of iron oxide nanoparticles. *Nanotechnol. Sci. Appl.* **2016**, *9*, 49–67. [[CrossRef](#)]
8. Khatavkar, S.N.; Sartale, S.D. α -Fe₂O₃ thin films by liquid phase deposition: Low-cost option for supercapacitor. *J. Solid State Electrochem.* **2017**, *21*, 2555–2566. [[CrossRef](#)]
9. Cornell, R.M.; Schwertmann, U. *The Iron Oxides: Structure, Properties, Reactions, Occurrence and Uses*, 2nd ed.; WILEY-VCH Verlag GmbH & Co. KGaA: Weinheim, Germany, 2003.
10. Liang, H.; Jiang, X.; Qi, Z.; Chen, W.; Wu, Z.; Xu, B.; Wang, Z.; Mi, J.; Li, Q. Hematite concave nanocubes and their superior catalytic activity for low temperature CO oxidation. *Nanoscale* **2014**, *6*, 7199. [[CrossRef](#)]
11. Yan, S.; Wu, Q. A novel structure for enhancing the sensitivity of gas sensors- α -Fe₂O₃ nanoropes containing a large amount of grain boundaries and their excellent ethanol sensing performance. *J. Mater. Chem. A* **2015**, *3*, 5982–5990. [[CrossRef](#)]
12. Marti, X.; Fina, I.; Jungwirth, T. Prospect for antiferromagnetic spintronics. *IEEE Trans. Magn.* **2015**, *51*, 18–21. [[CrossRef](#)]
13. Zeng, L.; Li, K.; Wang, H.; Yu, H.; Zhu, X.; Wei, Y.; Ning, P.; Shi, C.; Luo, Y. CO Oxidation on Au/ α -Fe₂O₃-Hollow Catalysts: General Synthesis and Structural Dependence. *J. Phys. Chem. C* **2017**, *121*, 12696–12710. [[CrossRef](#)]
14. Shen, S.; Lindley, S.A.; Chen, X.; Zhang, J.Z. Hematite heterostructures for photoelectrochemical water splitting: Rational materials design and charge carrier dynamics. *Energy Environ. Sci.* **2016**, *9*, 2744–2775. [[CrossRef](#)]
15. Schultz, A.M.; Salvador, P.A.; Rohrer, G.S. Enhanced photochemical activity of α -Fe₂O₃ films supported on SrTiO₃ substrates under visible light illumination. *Chem. Commun.* **2012**, *48*, 2012–2014. [[CrossRef](#)]
16. Aronniemi, M.; Lahtinen, J.; Hautojärvi, P. Characterization of iron oxide thin films. *Surf. Interface Anal.* **2004**, *36*, 1004–1006. [[CrossRef](#)]
17. Mirzaeian, M.; Ogbu, A.A.; Jirandehi, H.F.; Aidarova, S.; Ospanova, Z.; Tsendzughul, N. Surface characteristics of silver oxide thin film electrodes for supercapacitor applications. *Colloids Surf. A Physicochem. Eng. Asp.* **2017**, *519*, 223–230. [[CrossRef](#)]
18. Wang, L.; Lou, Z.; Deng, J.; Zhang, R.; Zhang, T. ethanol gas detection using a Yolk-Shell (Core-Shell) α -Fe₂O₃ nanospheres as sensing material. *ACS Appl. Mater. Interfaces* **2015**, *7*, 13098–13104. [[CrossRef](#)] [[PubMed](#)]
19. Cuong, N.D.; Hoa, T.T.; Khieu, D.Q.; Hoa, N.D.; Van Hieu, N. Gas sensor based on nanoporous hematite nanoparticles: Effect of synthesis pathways on morphology and gas sensing properties. *Curr. Appl. Phys.* **2012**, *12*, 1355–1360. [[CrossRef](#)]
20. Li, X.; Wei, W.; Wang, S.; Kuai, L.; Geng, B. Single-crystalline α -Fe₂O₃ oblique nanoparallelepipeds: High-yield synthesis, growth mechanism and structure enhanced gas-sensing properties. *Nanoscale* **2011**, *3*, 718–724. [[CrossRef](#)]
21. Hung, C.M.; Hoa, N.D.; Van Duy, N.; Van Toan, N.; Le, D.T.T.; Van Hieu, N. Synthesis and gas-sensing characteristics of α -Fe₂O₃ hollow balls. *J. Sci. Adv. Mater. Devices* **2016**, *1*, 45–50. [[CrossRef](#)]
22. Wang, L.; Wang, L.; Hu, H.; Truong, N.; Zhang, Y.; Schmuki, P.; Bi, Y. Plasmon-Induced hole-depletion layer on hematite nanoflake photoanodes for highly efficient solar water splitting nano energy plasmon-induced hole-depletion layer on hematite nano flake photoanodes for highly efficient solar water splitting. *Nano Energy* **2017**, *35*, 171–178. [[CrossRef](#)]
23. Gao, H.; Liu, C.; Jeong, H.E.; Yang, P. Plasmon-enhanced photocatalytic activity of iron oxide on gold nanopillars. *ACS Nano* **2012**, *6*, 234–240. [[CrossRef](#)]
24. Zhang, J.; Liu, X.; Wang, L.; Yang, T.; Guo, X.; Wu, S.; Wang, S.; Zhang, S. Au-functionalized hematite hybrid nanospindles: General synthesis, gas sensing and catalytic properties. *J. Phys. Chem. C* **2011**, *115*, 5352–5357. [[CrossRef](#)]
25. Thompson, C. V Solid-state dewetting of thin films. *Annu. Rev. Mater. Res.* **2012**, *42*, 399–434. [[CrossRef](#)]
26. Leroy, F.; Borowik, Ł.; Cheynis, F.; Almadori, Y.; Curiotto, S.; Trautmann, M.; Barbe, J.C.; Müller, P. How to control solid state dewetting: A short review. *Surf. Sci. Rep.* **2016**, *71*, 391–409. [[CrossRef](#)]
27. Serrano, A.; De La Fuente, O.R.; García, M.A. Extended and localized surface plasmons in annealed Au films on glass substrates. *J. Appl. Phys.* **2010**, *108*, 074303. [[CrossRef](#)]
28. Serrano, A.; Fernandez, J.F.; Rodriguez de la Fuente, O.; García, M.A. A novel route to obtain metal and oxide nanoparticles co-existing on a substrate. *Mater. Today Chem.* **2017**, *4*, 64–72. [[CrossRef](#)]
29. Gatel, C.; Snoeck, E. Epitaxial growth of Au and Pt on Fe₃O₄ (111) surface. *Surf. Sci.* **2007**, *601*, 1031–1039. [[CrossRef](#)]
30. Lachebi, I.; Fedala, A.; Djenizian, T.; Hadjersi, T.; Kechouane, M. Morphological and optical properties of aluminum nanoparticles deposited by thermal evaporation on heated substrates. *Surf. Coat. Technol.* **2018**, *343*, 160–165. [[CrossRef](#)]
31. Serrano, A.; Rubio-Zuazo, J.; López-Sánchez, J.; Enríquez, E.; Salas-Cólera, E.; Castro, G.R. Nanostructured Au(111)/Oxide epitaxial heterostructures with tailoring plasmonic response by a one-step strategy. *J. Phys. Chem. C* **2019**, *123*, 25294–25302. [[CrossRef](#)]
32. Serrano, A.; Llorca-Hernando, O.; Del Campo, A.; Rubio-Marcos, F.; Rodríguez de La Fuente, O.; Fernández, J.F.; García, M.A. Ag–AgO nanostructures on glass substrates by solid-state dewetting: From extended to localized surface plasmons. *J. Appl. Phys.* **2018**, *124*, 133103. [[CrossRef](#)]

33. Rubio-zuazo, J.; Ferrer, P.; López, A.; Gutiérrez-león, A.; Silva, I.; Castro, G.R. Nuclear instruments and methods in physics research a the multipurpose X-ray diffraction end-station of the BM25B-SpLine synchrotron beamline at the ESRF. *Nucl. Inst. Methods Phys. Res. A* **2013**, *716*, 23–28. [[CrossRef](#)]
34. Newville, M.; Ravel, B.; Haskel, D.; Rehra, J.J.; Stern, E.A.; Yacoby, Y. Analysis of multiple-scattering XAFS data using theoretical standards. *Phys. B Condens. Matter* **1995**, *208*, 154–156. [[CrossRef](#)]
35. Ravel, B.; Newville, M. ATHENA, ARTEMIS, HEPHAESTUS: Data analysis for X-ray absorption spectroscopy using IFEFFIT. *J. Synchrotron Radiat.* **2005**, *12*, 537–541. [[CrossRef](#)]
36. Sharma, S.K.; Spitz, J. Hilllock formation, hole growth and agglomeration in thin silver films. *Thin Solid Films* **1980**, *65*, 339–350. [[CrossRef](#)]
37. Serrano Rubio, A. *Modified Au-Based Nanomaterials Studied by Surface Plasmon Resonance Spectroscopy*; Springer: Berlin, Germany, 2015.
38. Serrano, A.; Rubio-Zuazo, J.; López-Sánchez, J.; Arnay, I.; Salas-Colera, E.; Castro, G.R. Stabilization of epitaxial α -Fe₂O₃ thin films grown by pulsed laser deposition on oxide substrates. *J. Phys. Chem. C* **2018**, *122*, 16042–16047. [[CrossRef](#)]
39. Rubio-Zuazo, J.; Onandia, L.; Salas-Colera, E.; Muñoz-Noval, A.; Castro, G.R. Incommensurate growth of thin and ultrathin films of single-phase Fe₃O₄(001) on SrTiO₃(001). *J. Phys. Chem. C* **2015**, *119*, 1108–1112. [[CrossRef](#)]
40. Malferrari, D.; Castellini, E.; Bernini, F.; Rubio, A.S.; Castro, G.R.; Sainz-Díaz, C.I.; Caleffi, M.; Brigatti, M.F.; Borsari, M. Chemical trapping of gaseous H₂S at high and low partial pressures by an iron complex immobilized inside the montmorillonite interlayer. *Microporous Mesoporous Mater.* **2018**, *265*, 8–17. [[CrossRef](#)]
41. Sanson, A.; Mathon, O.; Pascarelli, S. Local vibrational dynamics of hematite (α -Fe₂O₃) studied by extended X-ray absorption fine structure and molecular dynamics. *J. Chem. Phys.* **2014**, *140*, 224504. [[CrossRef](#)] [[PubMed](#)]
42. Oku, M.; Wagatsuma, K.; Matsuta, H. Background subtraction from transition metal 2p XPS by deconvolution using ligand atom XPS: Study on first transition metal cyanide complexes. *J. Electron Spectrosc. Relat. Phenom.* **1997**, *83*, 31–39. [[CrossRef](#)]
43. Mills, P.; Sullivan, J.L. A study of the core level electrons in iron and its three oxides by means of X-ray photoelectron spectroscopy. *J. Phys. D Appl. Phys.* **1983**, *16*, 723–732. [[CrossRef](#)]
44. Yamashita, T.; Hayes, P. Analysis of XPS spectra of Fe²⁺ and Fe³⁺ ions in oxide materials. *Appl. Surf. Sci.* **2008**, *254*, 2441–2449. [[CrossRef](#)]
45. Kruse, N.; Chenakin, S. XPS characterization of Au/TiO₂ catalysts: Binding energy assessment and irradiation effects. *Appl. Catal. A Gen.* **2011**, *391*, 367–376. [[CrossRef](#)]
46. Strohmeier, B.R. Copper/silver/gold alloy by XPS. *Surf. Sci. Spectra* **1994**, *3*, 175–181. [[CrossRef](#)]
47. Široký, K.; Jirešová, J.; Hudec, L.L.; Širok, K.; Jire, J. Iron oxide thin film gas sensor. *Thin Solid Films* **1994**, *245*, 211–214. [[CrossRef](#)]
48. Vuong, N.M.; Kim, D.; Kim, H. Surface gas sensing kinetics of a WO₃ nanowire sensor: Part 1—Oxidizing gases. *Sens. Actuators B Chem.* **2015**, *220*, 932–941. [[CrossRef](#)]
49. Vuong, N.M.; Kim, D.; Kim, H. Surface gas sensing kinetics of a WO₃ nanowire sensor: Part 2—Reducing gases. *Sens. Actuators B Chem.* **2016**, *224*, 425–433. [[CrossRef](#)]